Supporting Information for

Heterogeneous cation-lattice interaction and dynamics in triple cation perovskites revealed by infrared vibrational nanoscopy

Jun Nishida[1]**, Amani H. Alfaifi**[2,a]**, Thomas P. Gray**[1]**, Sean E. Shaheen**[3,4]**, and Markus B. Raschke**[1,*]

[1]Department of Physics, Department of Chemistry, and JILA, University of Colorado, Boulder, CO 80309, USA
[2]Department of Mechanical and Material Engineering, University of Denver, Denver, CO 80210, USA
[3]Department of Electrical, Computer, and Energy Engineering, and Department of Physics, University of Colorado, Boulder, CO 80309, USA
[4]Renewable and Sustainable Energy Institute, University of Colorado, Boulder, CO 80303, USA
[*]e-mail: markus.raschke@colorado.edu
[a]Present address: Department of Physics, Taif University, Taif 26571, Saudi Arabia

Supporting Information Contents

A. Synthesis and characterization of FAMACs perovskite

Preparation of FAMACs film as prepared. PbI_2 (99.9985%), $PbBr_2$ (99.999%), and CsI are purchased from Alfa Aesar. MABr, FAI, and MAI are purchased from Dyesol. Dimethyl formamide (DMF), dimethyl sulfoxide (DMSO), and chlorobenzene (CB) are obtained from Sigma-Aldrich and used as received. The ball-milled precursor salts and the chemical solvents are stored in N_2 glovebox (H_2O < 0.1 ppm, O_2 < 0.2 ppm). The microscope slides are purchased from Fisher scientific. The alloyed metal halide perovskite films are prepared as $[(FA_{0.83}MA_{0.17})_{0.95}Cs_{0.05}]Pb(I_{0.83}Br_{0.17})_3$ (abbreviated as FAMACs).[1] To have reproducible films, we use the method reported by Dou et al.[2] where ball-milled salts are store in an inert gas. The solution is made by mixing 100 mg of the ball-milled salts (1M of FAI, 1.1M of PbI_2, 0.2M of MABr, 0.2M of $PbBr_2$, and 0.05 M of CsI) in 130 μl of 1:3.3 v/v DMSO/ DMF mixture solvent. The FAMACs solution is spin-coated at 1000 r.p.m. for 10 seconds and then at 6000 r.p.m. for 20 seconds. About 7 seconds before the end of spin coating, a 150 μl of CB is dripped vertically onto the spinning substrate in a medium-speed, continuous stream. Then, the films are annealed at 100 °C on a hotplate for 1 hour. The PXRD pattern for the perovskite films thus prepared based on ball-milled salts confirms the black cubic phase of FAMACs.[2]

Preparation of water-vapor annealed FAMACs film. A FAMACs film as prepared is placed in a sealed container together with a filter paper wetted with saturated water solution of magnesium sulfate, which keeps the relative humidity inside the container to ~90% RH. After 36 hours, the film yields the water-vapor annealed sample as discussed in the main text. While we occasionally observe macroscopic defects accompanying a formation of PbI_2 crystal, such domains are easily identified and are avoided for the IR *s*-SNOM measurements (Fig. S1A).

UV-Vis and Photoluminescence spectra of the films. Figures S1B and S1C show visible absorption and photoluminescence (PL) spectra for the films as prepared and water-vapor annealed, characterized by a home-built UV-Vis and PL spectrometer. The optical bandgap derived in the film as prepared agrees well with the reported bandgap for the triple cation perovskite of ~1.63 eV. Upon the exposure to high humidity, with the slight red-shift in the bandgap (~1.61 eV), the perovskite films retain strong absorption together with the narrower line width in the PL, supporting that the corresponding domains remain in the
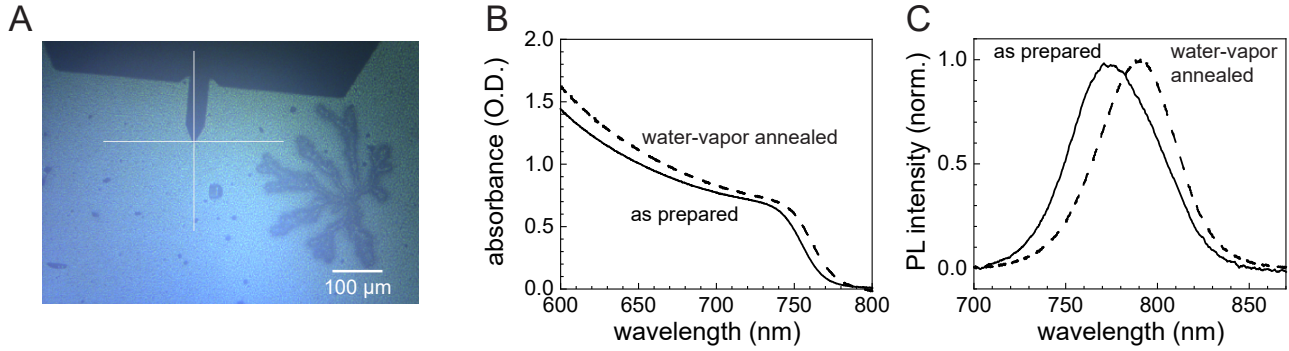
Figure S1: Water-vapor annealing. A. An optical image of a water-vapor annealed sample. The extended optically uniform surface corresponds to domains with homogeneously packed grains as discussed in the main text. We avoid the IR *s*-SNOM measurements on macroscopic defects with the dendroid patterns, which are only a minor fraction of the film. **B, C.** Visible absorption spectra (B) and photoluminescence spectra (C) for films as prepared and water-vapor annealed. The PL measurement for the water-vapor annealed sample is performed on the domains with the packed grains.

black cubic phase.

B. Infrared scattering scanning near-field optical microscopy (IR *s*-SNOM)

Mid-infrared pulsed laser system. A Yb:KGW oscillator (FLINT, Light Conversion) with a repetition rate of 76 MHz pumps a periodically-poled lithium niobate (PPLN) optical parametric oscillator (Levante OPO, APE Berlin). The difference frequency generation between the signal and idler outputs is performed using a AgGaS$_2$ crystal (HarmoniXX, APE Berlin) to yield mid-infrared pulses with a duration of ∼150 fs. The mid-infrared output spectrum is tunable from 5 μm (2000 cm^{-1}) to 10 μm (1000 cm^{-1}). For the work in this report, the center frequency of the mid-infrared output is set to ∼1715 cm^{-1} with the spectral bandwidth of ∼100 cm^{-1} FWHM and the pulse energy of ∼250 pJ. The pulse energy is further attenuated by mesh filters to <100 pJ and used for the subsequent IR *s*-SNOM experiments.

Infrared scattering scanning near-field optical microscopy (IR *s*-SNOM). The infrared pulses are directed to an IR *s*-SNOM system (Fig. S2, nanoIR2-s prototype, Anasys Instruments/Bruker), which is enclosed and purged with dry air (<1% RH). The *p*-polarized infrared pulse is focused on the apex of the gold-coated silicon tip (160AC-GG, NanoAndMore USA), using a 90° off-axis parabolic mirror (f = 25.4 mm, NA = 0.45). The scattered near-field signal is heterodyne amplified with a reference field on an HgCdTe detector (KLD-0.5-J1/11/, Kolmar Technologies). The electronic signal from the
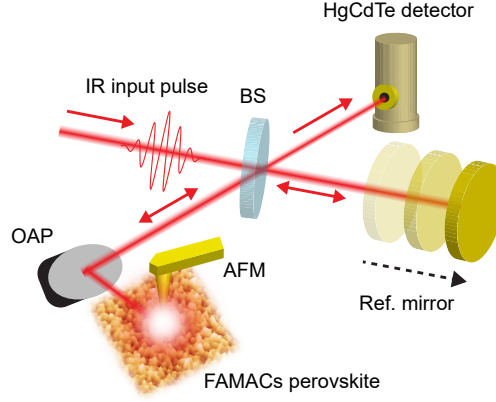
Figure S2: Schematic illustration of IR *s*-SNOM system. BS – beam splitter, OAP – off-axis parabolic mirror, AFM – atomic force microscope.

detector is demodulated with the second harmonics of the AFM tip tapping frequency using a lock-in amplifier (HF2LI, Zurich Instruments). To acquire the interferogram as shown in Fig 2A in the main text, the reference arm is scanned with a translation stage (ANT95-50-L-MP, Aerotech) with the velocity of 0.01 mm/s. Electronic TTL signals are generated every 300 nm of the stage motion to trigger the data acquisition by the lock-in amplifier with the averaging time constant of 17 ms.

IR *s*-SNOM hyperspectral mapping. The IR *s*-SNOM interferograms described above are acquired at $100-200$ different sample locations that are spatially separated by ~ 100 nm. The acquired interferograms are Fourier transformed, yielding near-field dispersive amplitude $A_{\mathrm{NF}}(\bar{\nu})$ and absorptive phase $\Phi_{\mathrm{NF}}(\bar{\nu})$ spectra. The $\Phi_{\mathrm{NF}}(\bar{\nu})$ spectra are referenced to a non-resonant flat gold surface and then baselined by second-order polynomials to isolate the narrowband vibrational resonance. The referenced and baselined line shapes are fit based on a Lorentzian vibrational resonance with the tip-sample near-field interaction taken into account using the point dipole model (PDM, see the following section C for details). The fitting parameters, i.e., vibrational peak area (A), peak position ($\bar{\nu}_0$), and line width (Γ), are then shown as two-dimensional images in Fig. 3A and 4A, which are constructed by cubic splining based on 100 and 225 data points, respectively.

C. Retrieval of complex dielectric function using the point dipole model (PDM)

As established, the observed absorptive line shape in the phase spectrum $\Phi_{\mathrm{NF}}(\bar{\nu})$ approximates the imaginary part of the complex dielectric function, yet details depend on the tip material and radius as well as
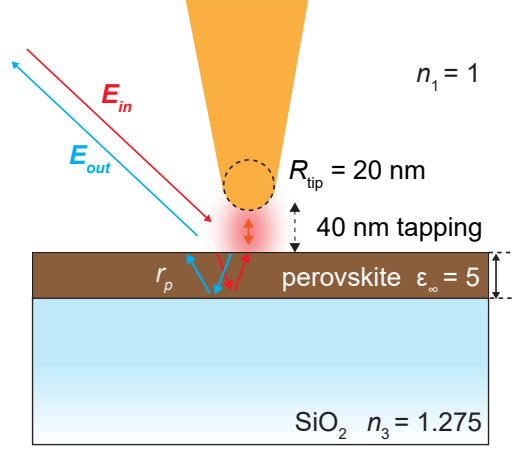
Figure S3: Modeling tip-sample near-field interaction. Sample configuration used for the fitting of the data based on the point dipole model (PDM).

the layer configuration of the sample.[3–5] This can be seen from the Lorentzian fit to $\Phi_{\mathrm{NF}}(\bar{\nu})$ (Fig. S4A), where the small deviation from the data is a result of the near-field tip-sample interaction.

We account for this scatter-induced distortion in the line shape using the established point dipole model (PDM), under consideration of the perovskite sample thickness of ~600 nm and the SiO$_2$ substrate (Fig. S3).[3,5,6] According to PDM,[3] the signal field E_{sig} scattered from a nanosphere as approximation for the tip apex in the proximity of a sample surface is given by $E_{\mathrm{sig}} \sim \alpha_{\mathrm{eff}} \cdot (1 + r_p)^2 \cdot E_{\mathrm{in}}$ with incident field E_{in}, complex reflection coefficient r_p for the p-polarized incident beam arising from the perovskite/SiO$_2$ layer, and effective polarizability α_{eff} given by

$$\alpha_{\mathrm{eff}} = \frac{\alpha_0}{1 - \dfrac{\alpha_0 \beta}{16\pi(R+z)^3}} \tag{1}$$

$\beta = (\varepsilon - 1)/(\varepsilon + 1)$ contains the complex dielectric function ε of the perovskite film. The radius of the nanosphere corresponding to the tip apex R is set to 20 nm, while the polarizability of the nanosphere is estimated as $\alpha_0 = 4\pi R^3 (\varepsilon_t - 1)/(\varepsilon_t + 2)$ with the dielectric constant of the tip material ε_t. E_{sig} is calculated for harmonic time-dependent modulation of the tip-sample distance z given by $z = z_A[1 - \cos(2\pi t)]/2$ with the tapping amplitude z_A of 40 nm, and the complex Fourier coefficient corresponding to the second harmonic modulation is calculated.[3,4,6] The near-field phase $\Phi_{\mathrm{NF}}^{\mathrm{calc.}}(\bar{\nu})$ function derived from the real and imaginary parts of the Fourier coefficient is then used to fit the observed phase spectrum $\Phi_{\mathrm{NF}}(\bar{\nu})$.[6]
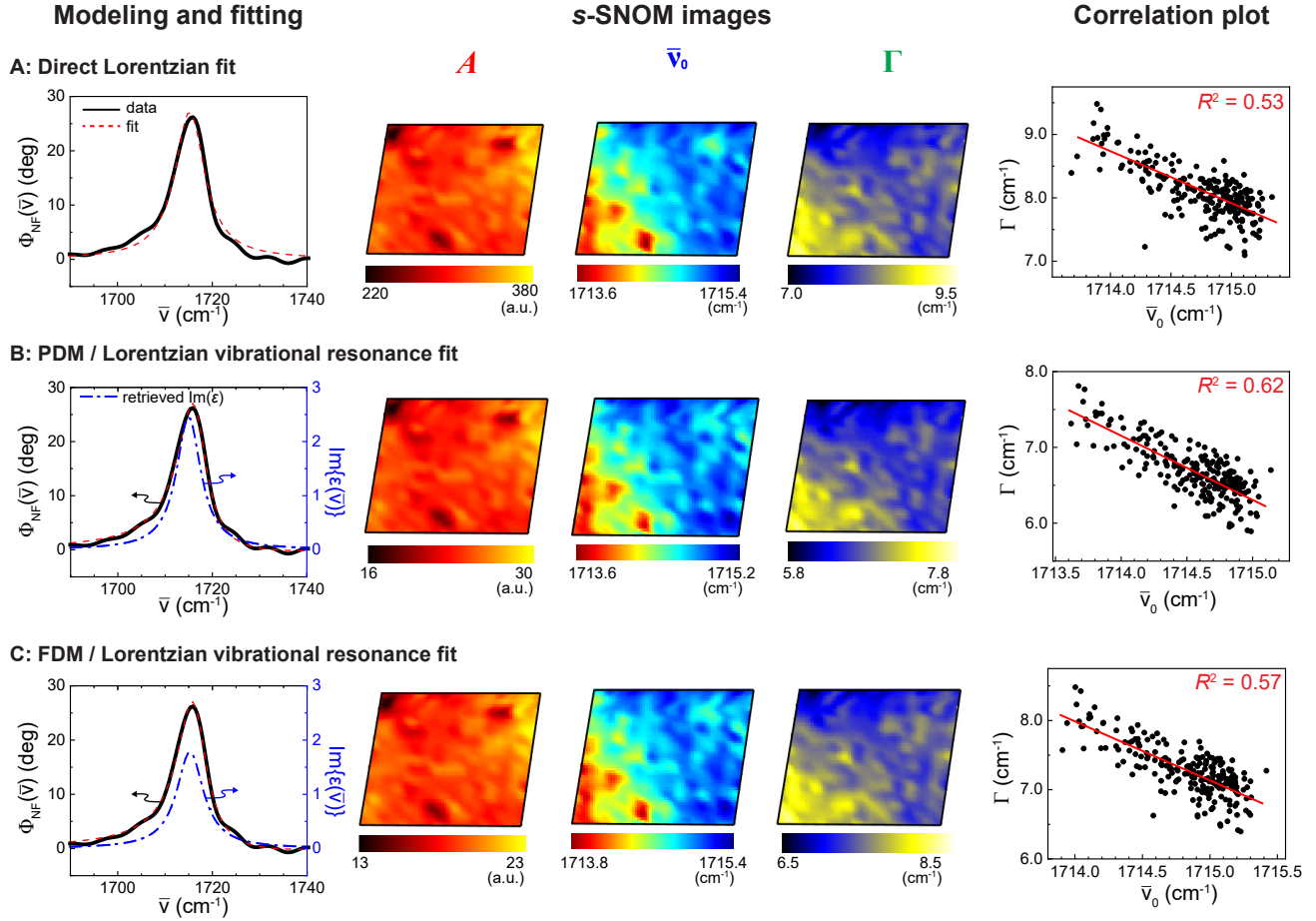
Figure S4: Retrieval of vibrational *s*-SNOM parameters. Left: The fits to the observed phase spectrum $\Phi_{NF}(\bar{\nu})$ and retrieved imaginary parts of the nano-localized dielectric function. **Middle:** the corresponding *s*-SNOM images based on the fittings. **Right:** the peak position $(\bar{\nu}_0)-$line width (Γ) correlations that are mainly discussed in the main text. Plots in each row is obtained by **(A)** Lorentzian fit directly to the observed phase spectrum $\Phi_{NF}(\bar{\nu})$, **(B)** the point dipole model (PDM) fit assuming the Lorentzian vibrational resonance, and **(C)** the finite dipole model (FDM) fit assuming the Lorentzian vibrational resonance.

We assume the dielectric function of the perovskite of the form $\varepsilon(\bar{\nu}) = \varepsilon_{nonres} + a/(\bar{\nu}_0{}^2 - \bar{\nu}^2 - i\Gamma\nu)$, where ε_{nonres} is the non-resonant dielectric constant and the second term describes the contribution from the Lorentzian vibrational resonance arising from the CN anti-symmetric vibration mode of the FA cation. ε_{nonres} is set to 5 at around $\sim 1715\ \mathrm{cm}^{-1}$ based on a previously reported infrared ellipsometry measurement on MAPbI$_3$ perovskite,[7] while a, $\bar{\nu}_0$ and Γ are varied as fitting parameters. The peak area A is then derived from the amplitude a and the line width Γ.

Fig. S4B shows the PDM fitting curve with the retrieved imaginary part of the dielectric function, the vibrational *s*-SNOM images, and the $\bar{\nu}_0-\Gamma$ correlation plots obtained. The PDM captures the asymmetric

line shape in the phase spectrum $\Phi_{\mathrm{NF}}(\bar{\nu})$, and the peak amplitude of the retrieved dielectric constant is consistent with the expected value.[7,8] The spatial variations and correlations obtained based on this fitting method are discussed in the main text.

We also find that the asymmetric phase spectrum $\Phi_{\mathrm{NF}}(\bar{\nu})$ is fit equally well based on the finite dipole model (FDM) established to derive the complex dielectric constant of, e.g., a polymer film at a similar frequency range ($\sim$1740 cm^{-1}) through the IR s-SNOM measurement.[3] As seen in Fig. S4C, while the absolute values of the retrieved A, $\bar{\nu}_0$, Γ are smaller by $\sim$25%, blue-shifted by $\sim$0.2 cm^{-1}, and broader by $\sim$0.7 cm^{-1}, respectively, than those from the PDM fitting, the length scale of the spatial variation and the negative $\bar{\nu}_0-\Gamma$ correlation are not affected, verifying that the main signatures of our observation are model independent.

Note that we calculate the reflection coefficient r_p using the three layer model, based on the nano-localized dielectric constant of the perovskite. This is a good approximation to r_p because the strong absorption by the CN anti-symmetric stretch mode heavily attenuates the incident field as it propagates deep into the perovskite film, rendering the dielectric constant in proximity of the tip a dominant contributor to the reflection.

D. IR s-SNOM vibrational parameters: correlation plots

Fig. S5 shows correlation plots of the different vibrational parameters extracted from the IR s-SNOM measurements, for both a film as prepared and a water-vapor annealed film. In particular, for the as-prepared samples with a larger set of data points (N = 1075), we do not observe significant correlations in peak area (A) – peak position ($\bar{\nu}_0$) and peak area (A) – line width (Γ) plots (Figs. S5A and S5B). Thus the FA cation density appears not to be a major factor determining the strength of the cation-lattice interaction and its associated vibrational dynamics. The peak position ($\bar{\nu}_0$) – line width (Γ) anti-correlations, on the other hand, are observed for the as prepared samples (Fig. S5C), with the potential underlying mechanism delineated in the main text. The water-vapor annealed films exhibit a similar behavior, i.e., the $A-\bar{\nu}_0$ and $A-\Gamma$ correlations are negligible (Figs. S5D and S5E), while the $\bar{\nu}_0-\Gamma$ anti-correlation is significant (Fig. S5F). Interestingly, the slopes for the linear $\bar{\nu}_0-\Gamma$ correlations are similar between the as prepared and water-vapor annealed films (Fig. S5C and S5F), suggesting the common mechanism of the $\bar{\nu}_0-\Gamma$

As prepared samples (N=1075)
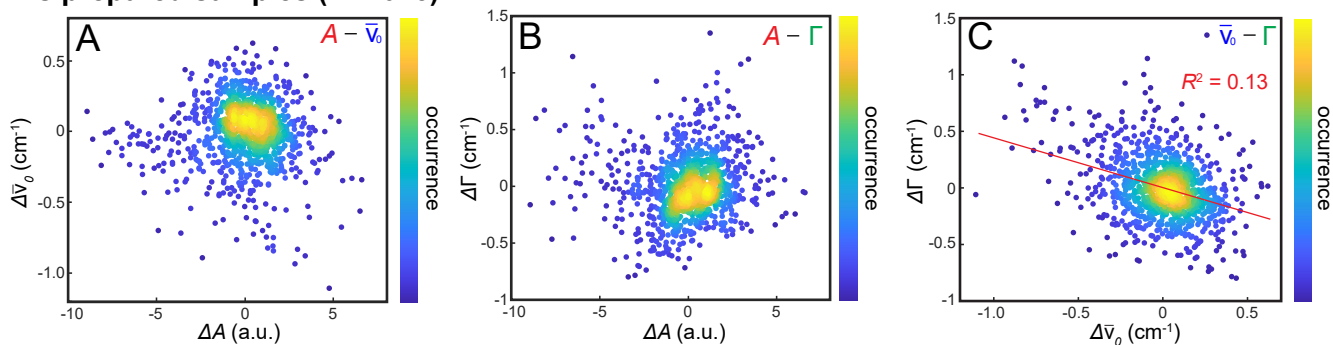
Water-vapor annealed samples (N=300)
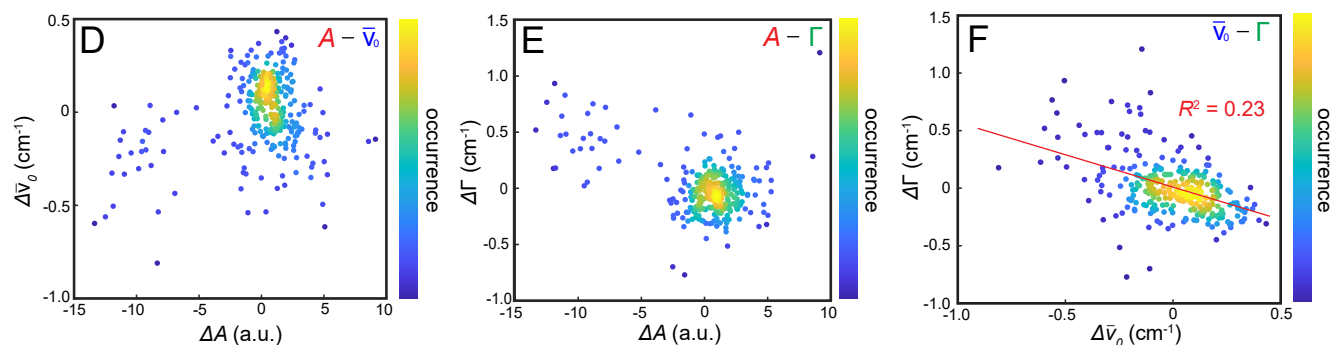
Figure S5: Correlation among vibrational parameters. **(A-C)** $A-\bar{\nu}_0$, $A-\Gamma$, and $\bar{\nu}_0-\Gamma$ correlation plots for the films as prepared. **(D-F)** The same correlation plots for the water-vapor annealed films.

variations for the two kinds of samples.

References

[1] M. Saliba, T. Matsui, J.-Y. Seo, K. Domanski, J.-P. Correa-Baena, M. K. Nazeeruddin, S. M. Zakeeruddin, W. Tress, A. Abate, A. Hagfeldt, M. Grätzel, *Energy Environ. Sci.* **2016**, *9*, 1989–1997.

[2] B. Dou, L. M. Wheeler, J. A. Christians, D. T. Moore, S. P. Harvey, J. J. Berry, F. S. Barnes, S. E. Shaheen, M. F. Van Hest, *ACS Energy Lett.* **2018**, *3*, 979–985.

[3] A. A. Govyadinov, I. Amenabar, F. Huth, P. S. Carney, R. Hillenbrand, *J. Phys. Chem. Lett.* **2013**, *4*, 1526–1531.

[4] A. S. McLeod, P Kelly, M. D. Goldflam, Z Gainsforth, A. J. Westphal, G. Dominguez, M. H. Thiemens, M. M. Fogler, D. N. Basov, *Phys. Rev. B* **2014**, *90*, 85136.

[5] E. A. Muller, B Pollard, M. B. Raschke, *J. Phys. Chem. Lett.* **2015**, *6*, 1275–1284.

[6] E. A. Muller, B. Pollard, H. A. Bechtel, P. V. Blerkom, M. B. Raschke, *Sci. Adv.* **2016**, *2*, e1601006.

[7] T. Glaser, C. Müller, M. Sendner, C. Krekeler, O. E. Semonin, T. D. Hull, O. Yaffe, J. S. Owen, W. Kowalsky, A. Pucci, R. Lovrinčić, *J. Phys. Chem. Lett.* **2015**, *6*, 2913–2918.

[8] V. C. A. Taylor, D. Tiwari, M. Duchi, P. M. Donaldson, I. P. Clark, D. J. Fermin, T. A. A. Oliver, *J. Phys. Chem. Lett.* **2018**, *9*, 895–901.